Oral presentation | Numerical methods
Numerical methods-IV
Wed. Jul 17, 2024 2:00 PM - 4:00 PM Room A

[8-A-01] Numerical investigation of the Block Spectral Stresses (BSS) method for turbulence modeling and shock-capturing

*Matteo Ruggeri[1], Victor C. B. Sousa[1], Carlo Scalo[1] (1. Purdue University)

Keywords: Turbulence modeling, Shock-capturing, Flux reconstruction, Block spectral method

Twelfth International Conference on Computational Fluid Dynamics (ICCFD12), Kobe, Japan, July 14-19, 2024

Numerical investigation of the Block Spectral Stresses (BSS) method for turbulence modeling and shock-capturing

M. Ruggeri*, V. C.B. Sousa** and C. Scalo**
Corresponding author: mruggeri@purdue.edu
* School of Aeronautics & Astronautics, Purdue University, West Lafayette, IN, USA.
** School of Mechanical Engineering, Purdue University, West Lafayette, IN, USA.

Abstract: The Block Spectral Stress (BSS) method is tested in its shock capturing capability, LES modeling, and both scenarios. The method is able to capture shocks in one-dimensions with numerical order up to 20, with good agreement between modeled and exact SFS stresses. The same approach is able to adequately preserve the hydrodynamic structure of a vortex impinging on a Mach 1.5 shock in two dimensions. In three-dimensional turbulent calculations the BSS method is compared against Smagorinsky and dynamic Smagorinsky all adapted to block spectral numerics. In Taylor-Green Vortex decay calculations $Re = 5,000$ and $M = 0.1$, the BSS model under-performs on coarse meshes (i.e. fewer mesh cell blocks) while over-performing on finer ones. Then the model is tested on a supersonic TGV problem with $Re = 1,600$ and $M = 1.5$, showing its capability to work as an LES and shock capturing method and keeping the same trend seen in the subsonic TGV case.. Finally, the limitations of block-spectral SFS closures are discussed.

Keywords: Turbulence modeling, Shock-capturing, Flux reconstruction, Block spectral method.

1 Introduction

The last years have seen the proliferation of block-spectral methods, which have the potential of combining the benefits of unstructured meshes with high-order numerical convergence [1, 2, 3, 4, 5, 6, 7, 8, 9, 10]. Spectral numerics are not robust in the presence of steep gradients [11, 12, 13], which are exacerbated by high-speed flow physics, which entail both strong shocks and highly compressible turbulence cascade effects [14, 15, 16]. Both shock and turbulence formation have a similar energy cascade dynamics [17, 18, 19]; differently from shocks, turbulence has a finite spectra therefore standard shock-capturing methods usually tend to remove a part of the spectra of the turbulence and therefore reduce the quality of the simulation. Instead, Eddy viscosity models–which allow to resolve turbulence on a coarser mesh than Direct Numerical Simulation quality (DNS) thanks to the modeling of small scales turbulence–are not able to fully dissipate the shock. This work aims to address these two problems with a unified model that is able to capture the shock and the same time does not remove a broad spectra of the turbulence from the simulation.

Block spectral methods can be implemented with three different approaches: the discontinuous Galerkin (DG) [20, 21, 22, 8, 23], the staggered grid approach (or spectral differences) [24, 6, 7], and the flux reconstruction (FR) method [2, 3, 4]. The latter is a more recent development in the field of block spectral numerics and serves as a basis for our work. It relies on correction (or lifting) functions that are used to propagate information from the block faces onto the interior solution points, effectively yielding a larger numerical stencil than just the inner-block numerics alone.

The trade-off between stability and accuracy of the FR method relies on the choice of the appropriate correction function. Asthana et al. [25] proved that even when the mesh is refined, the instabilities caused by aliasing errors related to the interpolation of the fluxes from the solution points to the faces are not completely reduced. In the same paper, they mathematically proved that traditional artificial viscosity strategies can stabilize the FR method for all numerical orders for sufficiently fine grids. They also showed how this allows to run 1D shock simulation up to numerical order 120, with the rate of convergence not being affected by the adoption of a shock sensor for localization of the artificial viscosity. The same order of accuracy was achieved by Sousa and Scalo [26] in one-dimensional Sod-shock-tube calculations with the FR method and the Legendre spectral viscosity (LSV) sub-filter scale closure. The latter is the inspiration for the current manuscript.

Tonnicello *et al.* [5] addressed the problem of reproducing the non-monotonic entropy profile across a captured shock [27, 28, 29, 30, 19] with high-order spectral differences. Most shock-capturing methods are unable to capture this phenomenon, returning a monotonic entropy rise across the shock. They compare Laplacian viscosity to a physical artificial viscosity method, showing that the latter is able to have a better prediction of the entropy even when the Laplacian approach is able to better capture the shock. The main drawback of the proposed approach is that it dissipates acoustic waves, which are critical for hypersonic boundary layer transition in canonical geometries. The authors pointed out that this is likely caused by the shock sensor and suggested that a divergence-based sensor may have better performance. However, previous authors [31, 32] that indeed used a divergence-based sensor, still witnessed spurious suppression of acoustic waves.

The current work investigates the performance of a combined SFS turbulence/shock-capturing model. Section 2 describes the code used for this investigation and the numerics used to solve the compressible Navier-Stokes equations. In the second part of the section the Block Spectral Stresses (BSS) model is described together with a description of the Smagorinsky and dynamic Smagorinsky models implemented with a block-spectral logic, and later used for comparison with BSS. Section 3 presents how the model performs in 1D and 2D shock-dominated flows. Then, the model's capability to capture SFS turbulence effects (i.e. act as a Large-Eddy Simulation closure) is tested in a subsonic Taylor-Green Vortex (TGV) flow 4. Finally, the model is tested on a supersonic TGV flow where it needs to work as an LES and shock capturing model 5.

2 Models description

The code used to perform the simulations in this manuscript is H^{3}AMR [33, 34, 35, 36, 37] (HySonic, High-Order, Hybrid Adaptive Mesh Refinement developed by HySonic Technologies, LLC) an unstructured block-spectral research code [38] for compressible flows based on flux reconstruction numerics [2]. In the current section, a description of the core numerics 2.1 and of various SFS models such as Smagorinsky [39] (Section 2.2.1), Dynamic Smagorinsky [40] (Section 2.2.2), and Block Spectral Stresses (BSS) (Section 2.2.3), as implemented in the code, are provided.

2.1 Code description (H3AMR)

The vector of conserved quantities reads:

$$\mathbf{Q} = \left[\rho,\ \rho u_1,\ \rho u_2,\ \rho u_3,\ \rho E\right]^T \tag{1}$$

where ρ is the density, u_i the velocity in the i^{th} direction in the physical space defined by the Cartesian coordinates (x_1, x_2, x_3), and $E = e + u_i u_i/2$ is the specific total energy, and $e = p/\rho(\gamma-1)$ is the specific internal energy for ideal calorically perfect gases. The flux vectors read:

$$\mathbf{F} = \begin{bmatrix} \rho u_1 \\ \rho u_1 u_1 + p - \mu\sigma_{11} \\ \rho u_1 u_2 - \mu\sigma_{12} \\ \rho u_1 u_3 - \mu\sigma_{13} \\ \rho(\rho e + p)u_1 - k\frac{\partial T}{\partial x_1} + \\ \cdots - \mu\sigma_{i1}u_i \end{bmatrix} \quad \mathbf{G} = \begin{bmatrix} \rho u_2 \\ \rho u_2 u_1 - \mu\sigma_{21} \\ \rho u_2 u_2 + p - \mu\sigma_{22} \\ \rho u_2 u_3 - \mu\sigma_{23} \\ \rho(\rho e + p)u_2 - k\frac{\partial T}{\partial x_2} + \\ \cdots - \mu\sigma_{i2}u_i \end{bmatrix} \quad \mathbf{H} = \begin{bmatrix} \rho u_3 \\ \rho u_3 u_1 - \mu\sigma_{31} \\ \rho u_3 u_2 - \mu\sigma_{32} \\ \rho u_3 u_3 + p - \mu\sigma_{33} \\ \rho(\rho e + p)u_3 - k\frac{\partial T}{\partial x_3} + \\ \cdots - \mu\sigma_{i3}u_i \end{bmatrix} \tag{2}$$

where μ is the dynamic viscosity, p the pressure, T the temperature, and $\sigma_{ij} = \frac{\partial u_i}{\partial x_j} + \frac{\partial u_j}{\partial x_i} - \delta_{ij}\frac{2}{3}\frac{\partial u_k}{\partial x_k}$ where δ_{ij} is the Kronecker delta. Given these vectors, the Navier-Stokes equations in physical space can be written as:

$$\frac{\partial \mathbf{Q}}{\partial t} + \frac{\partial \mathbf{F}}{\partial x_1} + \frac{\partial \mathbf{G}}{\partial x_2} + \frac{\partial \mathbf{H}}{\partial x_3} = 0 \tag{3}$$

The conservation equations can be recast in the computational space (ξ_1, ξ_2, ξ_3), with mapping defined separately for each mesh element, as:

$$
\begin{aligned}
Q &= J\mathbf{Q} \\
F &= J\left(\frac{\partial \xi_1}{\partial x_1}\mathbf{F} + \frac{\partial \xi_1}{\partial x_2}\mathbf{G} + \frac{\partial \xi_1}{\partial x_3}\mathbf{H}\right) \\
G &= J\left(\frac{\partial \xi_2}{\partial x_1}\mathbf{F} + \frac{\partial \xi_2}{\partial x_2}\mathbf{G} + \frac{\partial \xi_2}{\partial x_3}\mathbf{H}\right) \\
H &= J\left(\frac{\partial \xi_3}{\partial x_1}\mathbf{F} + \frac{\partial \xi_3}{\partial x_2}\mathbf{G} + \frac{\partial \xi_3}{\partial x_3}\mathbf{H}\right)
\end{aligned}
\tag{4}
$$

where italics are used for quantities transformed in the computational space; and $\partial \xi_i / \partial x_j$ is the Jacobian matrix for the linear transformation from the physical x_j to computational space ξ_i, and J is the determinant Jacobian of such matrix.

Therefore the Navier-Stokes equations can be rewritten as:

$$
\frac{\partial \mathbf{Q}}{\partial t} + \frac{1}{J}\frac{\partial F}{\partial \xi_1} + \frac{1}{J}\frac{\partial G}{\partial \xi_2} + \frac{1}{J}\frac{\partial H}{\partial \xi_3} = 0 \tag{5}
$$

which are the equations solved by H3AMR. Considering that J is constant over time we can divide all terms by it and keep $\mathbf{Q}$ in physical space.

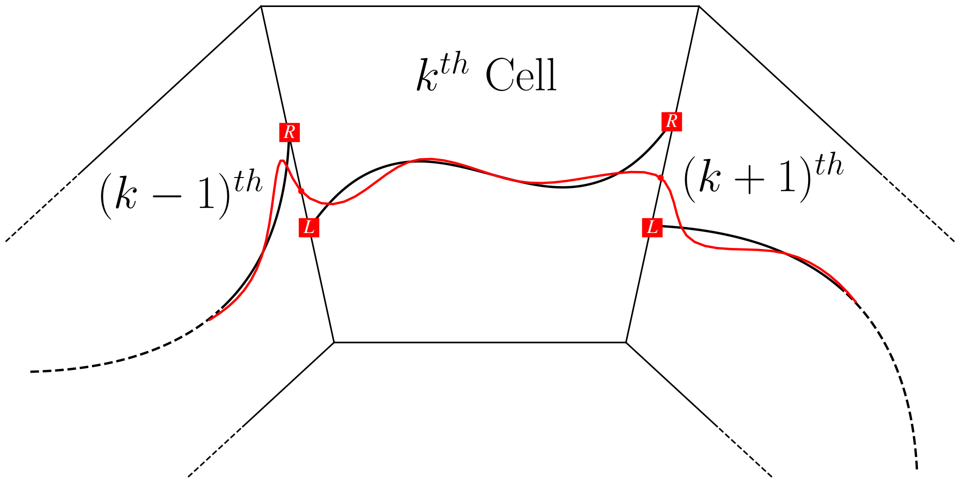

Figure 1: Example of 1D elements which are interpolate to the interface (black lines) and then corrected back to the solution points with their updated values at the interface (red line).

The computational domain is defined separately for each mesh element or block; in each element, the conserved quantities and the fluxes are stored in $N + 1$ Gauss-Legendre quadrature points or solution points per computational direction. This yields a polynomial reconstruction of order N, but an overall solver order of O=N+1 due to the intra-cell flux exchange. Hereafter, the numerical order (O) refers to the overall solver order, which is equal to the. number of solution points per cell.

For the sake of conciseness, the following numerical derivations will be explained with one-dimensional formulations; their 3D extension is simply derived via a tensorial concatenation of one-dimensional operators. Given a set of values of conserved quantities and fluxes on the solution points $f(\xi_j)$, their values are interpolated to the interfaces of the element ($f(-1)$ for the left interface and $f(+1)$ for the right interface along a given computational direction) and then updated to their new value using the Rusanov [41] method:

$$
\mathrm{F}^{new} = \frac{1}{2}(\mathrm{F}_R + \mathrm{F}_L) - \frac{S^+}{2}(\mathrm{Q}_R - \mathrm{Q}_L) \tag{6}
$$

where F^{new} is the new value of the flux at the interface, F_R and F_L are the initial values of the fluxes at the right and left of the interface, Q_R and Q_L are the initial values of the conserved quantities at the right and left of the interface, and S^+ is the maximum between the sum of the speed of sound a and velocity u at the left and right of the interface. From the updated values the derivatives can be computed using the flux reconstruction [2] method:

$$\frac{\partial f(\xi_i)}{\partial \xi} = D_{ij} f(\xi_j) + \left(f^{un}_{-\frac{1}{2}} - f(-1) \right) g'_L(\xi_i) + \left(f^{un}_{+\frac{1}{2}} - f(+1) \right) g'_R(\xi_i) \tag{7}$$

where $f^{un}_{-\frac{1}{2}}$ and $f^{un}_{+\frac{1}{2}}$ are the updated values at the left and right interface of the element, D_{ij} is the matrix representation of the first-order derivative, and $g'_L(\xi_i)$ and $g'_R(\xi_i)$ are the derivatives of the correction functions on the solution points. The correction functions have the property of being symmetric $g_R(\xi_j) = g_L(-\xi_j)$ and they can be computed from the Radau polynomials:

$$R_{R,N+1}(\xi_j) = \frac{(-1)^{N+1}}{2} \left(L_{N+1}(\xi_j) - L_N(\xi_j) \right), \tag{8}$$

where $R_{R,N+1}(\xi_j)$ and $L_{N+1}(\xi_j)$ are the Radau and Legendre polynomials of polynomial order $N+1$ at ξ_j. From the Radau polynomials, the correction functions can be computed as:

$$g_{N+1} = \frac{N+1}{2N+1} R_{R,N+1} + \frac{N}{2N+1} R_{R,N}. \tag{9}$$

Figure 1 shows how this process works, where the black line shows the interpolation to the interface of the element. Then, the values at the interface are updated to a new common value which is the red dot at the interface. The updated quantity is interpolated back to the solution points making the reconstruction inside the element C^0 continuous among elements.

2.2 Filtered Navier-Stokes formalism

The Navier-Stokes equations in the physical space can be filtered with a spatial filter, indicated with an overbar $\overline{(\cdot)}$, which is assumed to commute with the derivative operation. For compressible flows it is suggested to use a Favre-based filter:

$$\check{f} = \frac{\overline{\rho f}}{\overline{\rho}}, \tag{10}$$

which leads to the Favre-filtered Navier-Stokes equations:

$$\frac{\partial \overline{\rho}}{\partial t} + \frac{\partial \overline{\rho} \check{u}_j}{\partial x_j} = 0 \tag{11}$$

$$\frac{\partial \overline{\rho} \check{u}_i}{\partial t} + \frac{\partial}{\partial x_j} \left(\overline{\rho} \check{u}_i \check{u}_j + \overline{p} \delta_{ij} - \mu \check{\sigma}_{ij} + \overline{\rho} \tau_{ij} \right) = 0, \tag{12}$$

$$\frac{\partial \overline{E}}{\partial t} + \frac{\partial}{\partial x_j} \left((\overline{E} + \overline{p}) \check{u}_j - k \frac{\partial \check{T}}{\partial x_j} - \mu \check{\sigma}_{ij} \check{u}_i + \frac{1}{2} \left(\frac{\gamma \pi_j}{\gamma - 1} + \overline{\rho} C_p q_j \right) + \frac{1}{2} \overline{\rho} \zeta_j \right) = \mu \epsilon, \tag{13}$$

$$\frac{\overline{p}}{\gamma - 1} = \overline{E} - \frac{1}{2} \overline{\rho} \check{u}_i \check{u}_i - \frac{1}{2} \overline{\rho} \tau_{ii}. \tag{14}$$

The last is the state equation in the case of an ideal gas, k and C_p are the thermal conductivity and heat capacity at a constant pressure of the gas. The filtering operation yields the unclosed SFS terms: the SFS stress tensor τ_{ij}, the SFS heat flux q_j, the SFS pressure-work π_j, the SFS kinetic energy advection ζ_j, and the SFS heat dissipation ϵ. The last two terms are small and can be considered negligible for this reason they are not considered in most of the existing LES models. The Smagorinsky and Dynamic Smagorisky models assume negligible also the SFS pressure-work π_j, which is instead modeled by the BSS method because leads to better results when the model is used for shock-capturing. The quantities can be analytically computed as:

$$\tau_{ij} = \widetilde{u_i u_j} - \check{u}_i \check{u}_j \tag{15}$$

$$q_j = \widetilde{T u_j} - \check{T} \check{u}_j \tag{16}$$

$$\pi_j = \overline{p u_j} - \overline{p} \check{u}_j \tag{17}$$

$$\zeta_j = \widetilde{u_k u_k u_j} - \check{u}_k \check{u}_k \check{u}_j \tag{18}$$

$$\epsilon = \frac{\partial \overline{\sigma_{ij} u_i}}{\partial x_j} - \frac{\partial \check{\sigma}_{ij} \check{u}_i}{\partial x_j} \tag{19}$$

In the following, three alternative SFS models are formulated in the computational space, consistently with the implementation of BSS into H3AMR.

$$\mathbf{F}_j^{\mathrm{SFS}} = \begin{bmatrix} 0 \\ \bar{\rho}\tau_{11} \\ \bar{\rho}\tau_{12} \\ \bar{\rho}\tau_{13} \\ \frac{1}{2}\left(\frac{\gamma\pi_1}{\gamma-1} + \bar{\rho}C_p q_1\right) \end{bmatrix} \mathbf{G}_j^{\mathrm{SFS}} = \begin{bmatrix} 0 \\ \bar{\rho}\tau_{21} \\ \bar{\rho}\tau_{22} \\ \bar{\rho}\tau_{23} \\ \frac{1}{2}\left(\frac{\gamma\pi_2}{\gamma-1} + \bar{\rho}C_p q_2\right) \end{bmatrix} \mathbf{H}_j^{\mathrm{SFS}} = \begin{bmatrix} 0 \\ \bar{\rho}\tau_{31} \\ \bar{\rho}\tau_{32} \\ \bar{\rho}\tau_{33} \\ \frac{1}{2}\left(\frac{\gamma\pi_3}{\gamma-1} + \bar{\rho}C_p q_3\right) \end{bmatrix} \tag{20}$$

and then the code continues to work as described in 2.1.

2.2.1 Smagorinsky

Smagorisky [39] proposed a model to close the filtered Navier-Stokes equations based on the resolved strain-rate tensor. The model was developed for incompressible flows and hence closing only τ_{ij}, but it can be extended to compressible flows with at least a closure for q_j. The model relies on the eddy viscosity which is computed as:

$$\nu_t = 2C\Delta^2|\check{S}| \tag{21}$$

where $C = 0.0256$ is the Smagorinsky constant, Δ is (in our case) the characteristic computational length scale is

$$|\check{S}| = \sqrt{2\check{S}_{ij}\check{S}_{ij}} \tag{22}$$

the norm of the strain-rate tensor, and $\check{S}_{ij}$ is the strain-rate tensor, which is computed using the computational-space derivatives as

$$\check{S}_{ij} = \frac{1}{2}\left(\frac{\partial \check{u}_i}{\partial \xi_j} + \frac{\partial \check{u}_j}{\partial \xi_i}\right). \tag{23}$$

The computational length scale Δ can be estimated as $\Delta = \sqrt[3]{w_i w_j w_k}$ where w_i, w_j, and w_k are respectively the Gauss-Legendre quadrature weights in the i-th, j-th, and k-th computational directions. For an orthogonal mesh, this formulation matches the one in physical space, provided the spatial length scale is the physical one.

From the eddy viscosity the SFS stress tensor can be computed as:

$$\tau_{ij} = -\nu_t(\check{S}_{ij} - \frac{1}{3}\check{S}_{kk}\delta_{ij}) \tag{24}$$

where δ_{ij} is the Kronecker delta. The SFS heat flux can be computed as:

$$q_j = -\frac{\nu_t}{Pr_t}\frac{\partial \check{T}}{\partial \xi_j} \tag{25}$$

where $Pr_t = 0.9$ is the turbulent Prandtl number and it is assumed to be constant in this formulation.

2.2.2 Dynamic Smagorinsky

To overcome the overly dissipative nature of the Smagorinsky model, Germano *et al.* [42] developed a dynamic model, capable of modulating its intensity based on the local and instantaneous levels of turbulence. The original model was proposed for incompressible flow by Germano et al. [42] and then extended to compressible flow by Moin *et al.* [40]. The Dynamic Smagorinsky model is based on the standard Smagorinsky model but instead of assuming C and Pr_t constant, they are computed dynamically according to equations 15 and 19 in [40] derived from algebraic identities, which entail numerous auxiliary test-filtering operations. The model was developed to work with finite-difference or finite-volume codes, but was never applied to block-spectral numerical codes. Therefore, each element is treated on its own and it has a specific value of C and Pr_t. Because of the small domain covered by the elements it can happen that the constants are negative, therefore the code imposes a lower limit of 0 for C and 0.01 for Pr_t.

2.2.3 Block Spectral Stresses (BSS)

The Block-Spectral Stresses (BSS) method builds upon the Legendre-Spectral Viscosity (LSV) closure of Sousa and Scalo [26], and specifically redesigned for a block-spectral code. The LSV closure was only tested against shock-dominated flows.

The BSS model estimates the high-wavenumber resolved kinetic energy block-by-block using the gradient of the velocity in each solution point:

$$E_N^i(\check{u}_j) = \left| \frac{1}{\gamma_N} \sum_{k=0}^{N} \left(\ell_j \frac{\partial \check{u}_j(\xi_k^i)}{\partial \xi_i} \right)^2 L_N(\xi_k^i) w_k \right| \tag{26}$$

where $\partial \check{u}_j(\xi_k^i)/\partial x_i$ is the computational derivative of $\check{u}_j$ along the i direction computed with the correction polynomials, $L_N(\xi_k^i)$ is the value of the highest Legendre mode at ξ_k^i (i is the direction in which the value is filtered), w_k is the Gauss Legendre quadrature weight, ℓ^j is the computational length scale of the solution point (which in the computational space is equal to w_j), $\gamma_N = 2/(2N+1)$, and N is the polynomial order of the function used to reconstruct the solution inside the element. The BSS method has better shock-capturing capability than LSV and yields SFS stresses more closely resembling the exact values. LSV stresses, for example, do not preserve the symmetric structure of SFS stresses of two-dimensional vortex, because the cutoff energy was computed from $\check{u}_j(\xi_k^i)^2$ instead of using the derivative. Finally, using the derivative of the velocity field guarantees Galilean invariance.

From the estimated cutoff energy, it is possible to compute the SFS scale $v_i(\check{u}_j) = \sqrt{\frac{N}{2} E_N^i(\check{u}_j)}$, where the factor $N/2$ is the average grid spacing of the element in computational space. From that it is possible to estimate the dissipation needed by the model with a mixing-length arguement,

$$\mathcal{D}_{ij} = v_i(\check{u}_j)\ell_j. \tag{27}$$

The SFS quantities can then be computed as:

$$\tau_{ij} = -C_{ij} \frac{1}{2} \left(\mathcal{D}_{ij} \frac{\partial \check{u}_i}{\partial \xi_j} + \mathcal{D}_{ji} \frac{\partial \check{u}_j}{\partial \xi_i} \right) \tag{28}$$

$$q_j = -C_q \mathrm{diag}(\mathcal{D})_j \frac{\partial \check{T}}{\partial \xi_j} \tag{29}$$

$$\pi_j = -C_p \mathrm{diag}(\mathcal{D})_j \frac{\partial \bar{p}}{\partial \xi_j} \tag{30}$$

where $\mathrm{diag}(\mathcal{D})$ is the vector of the diagonal of (27). The summation over repeated indices is not implied. C_q and C_p are constants, and C_{ij} is a matrix of constants, with values reported in table 1. Unlike the Smagorinsky model, the diagonal of the strain-rate tensor is not removed, as it provides the normal SFS stresses that support the shock-capturing capabilities of the model. The BSS closure does not modulate the SFS stresses in the spectral space like LSV does.

C_{ii}	$C_{i\neq j}$	C_q	C_p
1.0	0.2	1.0	1.0

Table 1: Coefficients of equations (28, 29, 30). Where the first two are the coefficients of a constant matrix respectively at the diagonal and off-diagonal. The last two are single constant coefficients.

3 BSS shock capturing capability

In this section we are going to assess BSS's capability to act as a shock-capturing closure, in a one-dimensional Sod-shock tube problem (Section 3.1) and a two-dimensional shock vortex interaction case (Section 3.2).

3.1 Sod shock tube

The Sod-shock tube [43] is a standard case widely used to test shock-capturing methods [44, 45, 26]. The case simulates a tube with a gas with higher pressure and density on the left and lower values on the right separated by a membrane at $x = 0$, that is removed at time zero. A shock and an expansion wave form, propagating respectively to the right and to the left of the membrane. The problem is described by the Euler equations with (normalized) initial conditions:

$$[u_1, p, \rho] = \begin{cases} [0, 1, 1] & \text{if } x \leqslant 0 \\ [0, 0.1, 0.125] & \text{if } \quad x > 0 \end{cases} \tag{31}$$

where u_1 is the velocity, p the pressure, and ρ the density. The toughest numerical challenge for the high-order scheme is given by the shock and the contact discontinuity.

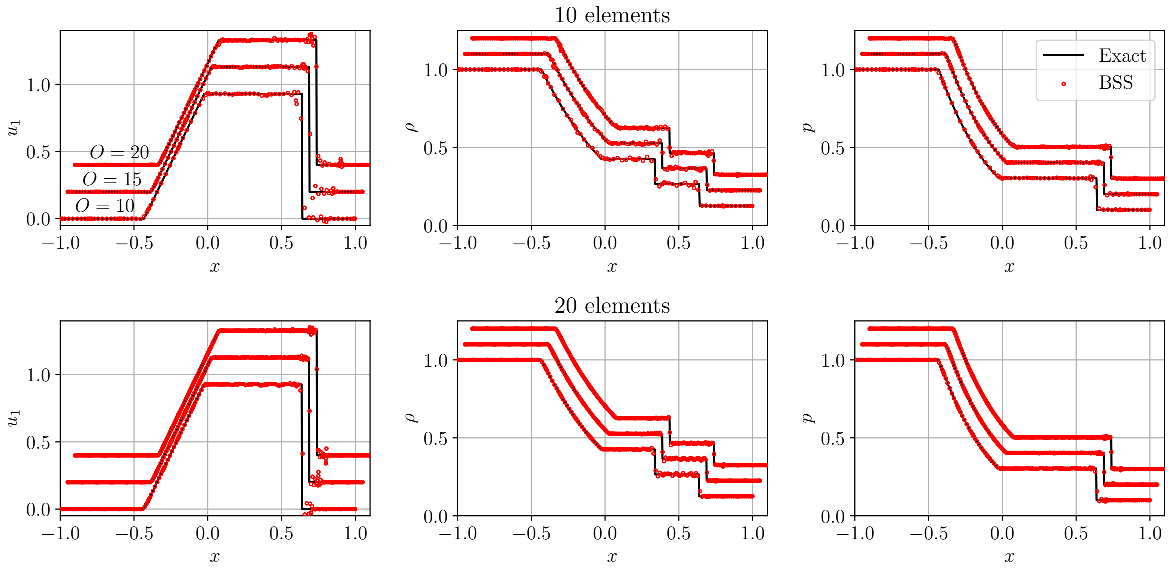

Figure 2: Sod shock tube [43] velocity u_1, density ρ and pressure p at $t = 0.264$ s. The first row has a domain of 10 elements and the second of 20 elements. Inside each element the solution is reconstructed with solver accuracy (O=) of 10, 15, and 20 (which correspond to 100, 150, and 200 DOF on the first row and 200, 300, and 400 DOF on the second row).

Figure 2 compares the velocity, pressure, and density profiles at $t = 0.264$ s of the simulated case with BSS and the analytical solution on different mesh and numerical order O resolution. On the top row the results are obtained using 10 mesh elements and in each plot the numerical order is O=10, 15, and 20 from the bottom to the top. Most of the oscillation around the shock is visible in the velocity profile, whereas the pressure looks mostly smooth. Increasing the numerical order sharpens the shock, reduces the post-shock oscillations while increasing the pre-shock ones. However, this phenomenon is not dependent on the shock itself but on its proximity to the inter-block boundary. The bottom row of Figure 2 presents results obtained on a mesh with 20 elements. The most visible outcome is the fact that the oscillation are reduced when compared to the same numerical order, on a finer domain, and also allows a better capturing of the shock. Therefore, it is possible to conclude that increasing the number of degrees of freedom (DOF), i.e. total number of solution points, reduces the oscillation cased by the shock, but to have a better resolution of the shock it is better to increase the number of elements and not only the numerical order.

Figure 3 shows the velocity, pressure, density, SFS stresses, SFS heat flux, and SFS pressure-work for 10 mesh elements and numerical order 20. The exact SFS quantities are computed using equations (28-30) on the analytical solution on the same mesh with numerical order 72 filtered down to 20 and the BSS one are obtained *a posteriori*. As expected, considering that the shock has an infinite spectra the exact SFS quantities exhibit point-to-point oscillations in the Legendre spectral space η. The modeled SFS quantities follow very closely the exact ones. The last row, shows the Legendre transform of the *a posteriori* versus exact SFS stresses, SFS heat flux, and SFS pressure-work in the element with shock. For all cases, the spectra of the SFS *a posteriori* match the behavior of the exact solution spectra, with the oscillation of sign and similar magnitude. There are some differences in the spectra of the SFS stresses but it is possible to see that this difference is due to the discrete nature of the investigation, indeed if the results were continuous the exact solution spectra would oscillate further.

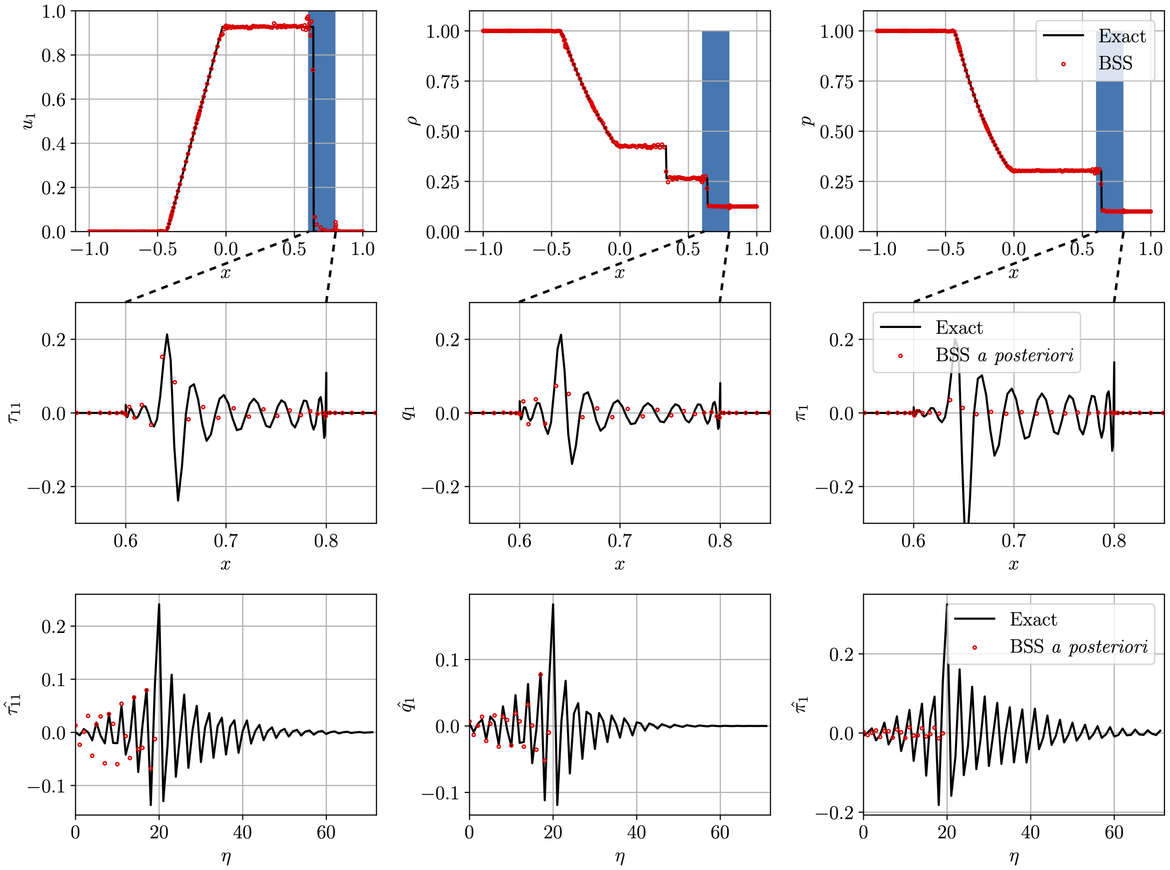

Figure 3: Top row: Sod-shock tube [43] velocity u_1, density ρ, pressure p, SFS stresses τ_{11}, SFS heat flux q_1, and SFS pressure-work π_1 at $t = 0.264$ s, for a 10 elements mesh with numerical order $O = 20$. Middle row: SFS stresses computed using equations 28-30. Bottom row: Legendre transform of the three SFS quantities computed in the element with the shock. Solid lines are exact values, while red circles are the *a posteriori* quantities.

3.2 Shock vortex interaction

This section investigates the interaction between a vortex with zero-net circulation and a steady shock. For this investigation the domain is $[0, 2L] \times [0, L]$, the freestream velocity before the shock is $V_0 = 1.5\sqrt{\gamma p_0/\rho_0}$, the initial shock location is $x_s/L = 1/2$, and the vortex center at $x_{cv}/L = 1/4$ and $y_{cv}/L = 1/2$.

The expression of the vortex-induced tangential velocity

$$\frac{u_\theta(r)}{u_\theta(a)} = \begin{cases} \frac{r}{a}, & \text{if } r \leqslant a \\ \frac{\eta}{2}\left(\frac{r}{b} - \frac{b}{r}\right), & \text{if } a < r \leqslant b \\ 0, & \text{otherwise,} \end{cases} \tag{32}$$

differentiates between an inner circle $r \leqslant a$ and an outer ring $a < r \leqslant b$, where $a/L = 0.075$, $b/L = 0.175$ and $\eta = 2(b/a)/[1 - (b/a)^2]$. The total velocity is $\mathbf{u} = u_\theta(r)\hat{\mathbf{e}}_\theta + V_0\hat{\mathbf{e}}_x$ where the maximum tangential velocity is $u_\theta(a) = 0.9V_0$. The pressure field is derived from ideal gas and isentropic relations, and its gradient is taken to balance the centrifugal forces:

$$\frac{\partial P}{\partial r} = \rho\frac{u_\theta^2(r)}{r}, \quad P = \rho RT, \quad \frac{P}{P_0} = \left(\frac{\rho}{\rho_0}\right)^\gamma. \tag{33}$$

Other works [46, 47, 5] that have performed simulations on this problem reported that the interaction of the vortex with shock leads to the creation of two smaller vortices with the upper one in a forward position respect to the lower one. Figure 4 shows the evolution of the vortex passing through the shock deforming the shock into an S-shape.

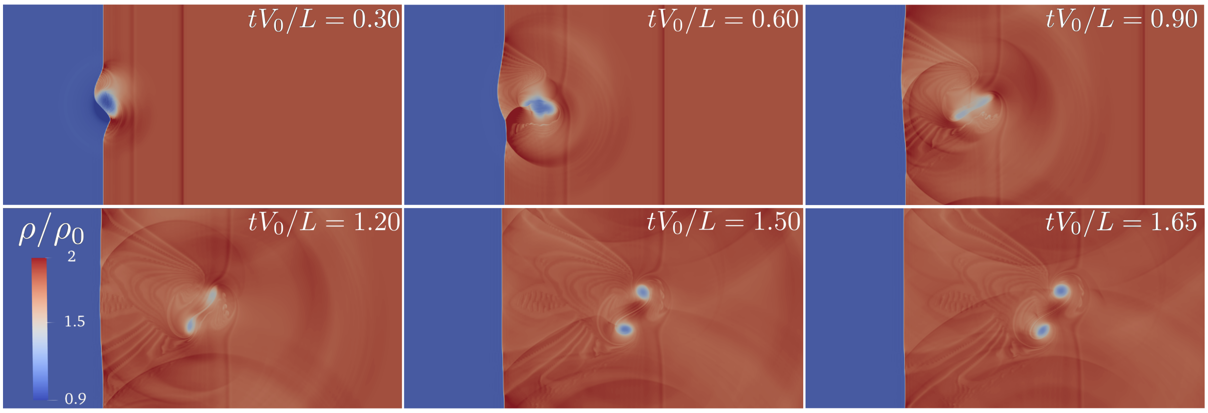

Figure 4: Shock-vortex interaction evolution using numerical order $O = 4$ and a mesh 256x128 blocks (524,768 DOF).

Figure 5 shows the effects of increasing numerical order (along the rows) and increasing mesh refinementment (in the columns). The total number of degrees of freedom DOF is kept constant along each row increasing their number of a factor of 4. As previously seen in the Sod-shock tube investigation, when the total number of degrees of freedom is the same, the simulation with the lowest numerical order (i.e. highest mesh-element count) has the best result. This is most evident in the middle row results, where increasing the numerical order to $O = 16$, while keeping the DOFs the same at 131072, reduces the quality of the numerical solution. At 524,288 DOFs, there is little variation in the numerical solution when trading mesh refinement with polynomial refinement.

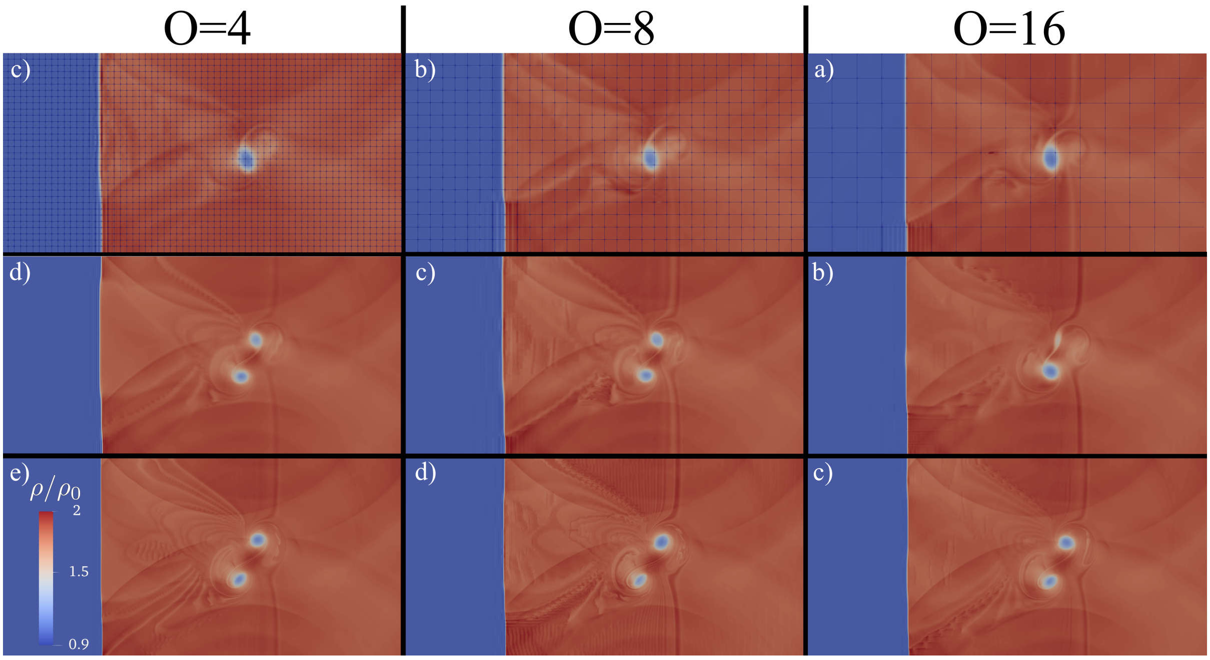

Figure 5: Shock-vortex interaction at $tV_0/L = 1.65$ with different numerical order and mesh resolution. Top row (for all columns): 32768 DOFs ; Middle row: 131072 DOFs; Bottom row: 524288 DOFs. The meshes have in x and y: a) 16x8, b) 32x16, c) 64x32, d) 128x64, and e) 256x128.

4 Subfilter-Scale modeling: Taylor-Green Vortex (TGV)

The Taylor-Green Vortex (TGV) is a three-dimensional flow in a triply-period box, exhibiting turbulent breakdown and relaxation towards decaying homogeneous isotropic turbulence. The simulation starts at

$t = 0$ s and ends at $t = 200$ s in a $[-\pi L, \pi L]^3$ domain with the following initial conditions:

$$\rho(\mathbf{x}, 0)/\rho_0 = 1, \tag{34}$$

$$\frac{u_1(\mathbf{x}, 0)}{V_0} = \sin\left(\frac{x_1}{L}\right)\cos\left(\frac{x_2}{L}\right)\cos\left(\frac{x_3}{L}\right), \tag{35}$$

$$\frac{u_2(\mathbf{x}, 0)}{V_0} = -\cos\left(\frac{x_1}{L}\right)\sin\left(\frac{x_2}{L}\right)\cos\left(\frac{x_3}{L}\right), \tag{36}$$

$$\frac{u_3(\mathbf{x}, 0)}{V_0} = 0, \tag{37}$$

$$\frac{p(\mathbf{x}, 0)}{\rho_0 V_0^2} = \frac{p_0}{\rho_0 V_0^2} + \frac{1}{16}\left[\cos\left(\frac{2x_1}{L}\right) + \cos\left(\frac{2x_2}{L}\right)\right]\left[\cos\left(\frac{2x_3}{L}\right) + 2\right] \tag{38}$$

where $\rho_0 = 1$, $V_0 = 0.1$, $p_0 = 1/\gamma$, and $L = 1$ are the non-dimensionalized density, velocity, pressure, and length scale. The Mach number of the flow is $M_0 = V_0 / \sqrt{\gamma p_0/\rho_0} = 0.1$. The Reynolds number is $Re = \rho_0 V_0 L / \mu_0 = 5000$ where the viscosity is considered to be constant at $\mu_0 = 2 \cdot 10^{-5}$. All the simulations use a third-order Runge-Kutta time advancement method with $CFL = 0.1$. Grid convergence is achieved on a 32^3 elements mesh with numerical order O=9.

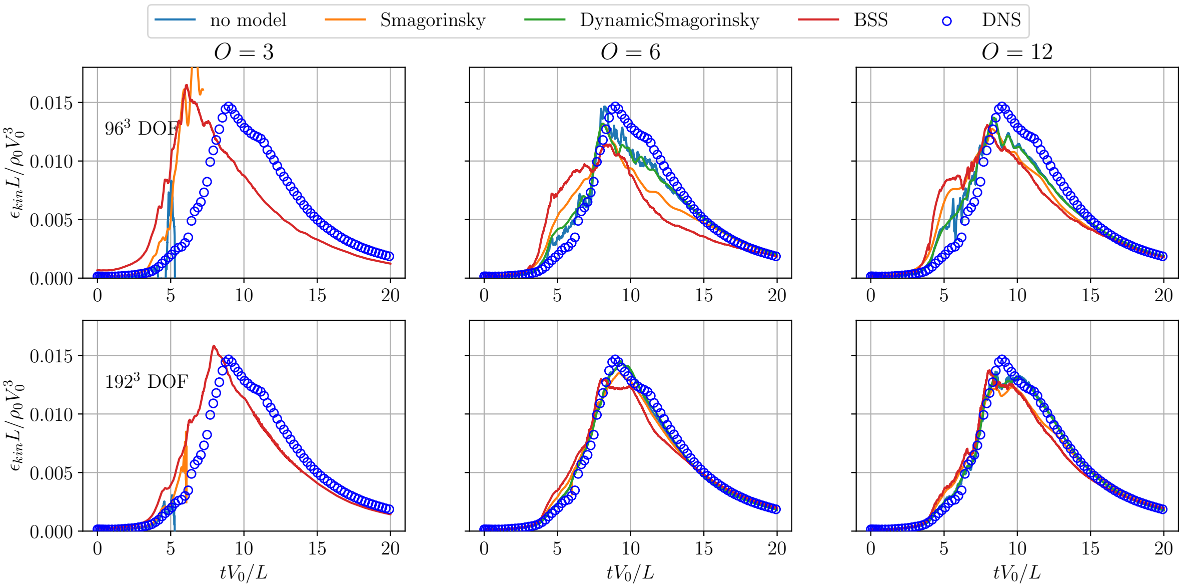

Figure 6: Normalized time and dissipation ϵ_{kin} with different degrees of freedom (DOF) and numerical order. From left to right the meshes use for the 96^3 DOF case have respectively 32^3, 16^3, and 8^3 elements. For the 192^3 DOF respectively 64^3, 32^3, and 16^3 elements. Solid lines are the simulations performed with LES models, while blue circles are the DNS results.

Similarly to the shock-vortex interaction case, figure 6 reports how the dissipation predicted by different methods behaves by varying the degrees of freedom (DOF) and numerical orders. When using numerical order 3 only BSS is able to yield stable results, whereas the other methods lead to blow up. Differently from spectral method, where the blow up is caused by the dissipation becoming negative, in block spectral code the blow up is caused by oscillations in the single block which in some cases can be seen in the global statistics as the dissipation. When running with 96^3 DOFs the BSS is significantly more dissipative than the other methods, especially when turbulent break down is initiated, and consequently the peak dissipation is smaller than the other methods. In the 192^3 DOF case, BSS is the only method able to capture the plateau after the peak. The profile of the dynamic Smagorinsky method is similar to the profile without any model but without the oscillation present in the latter curve. This result is caused by the fact that the model is applied on a block-by-block nature therefore it has a small effect on the simulation but is strong enough to filter down the solution.

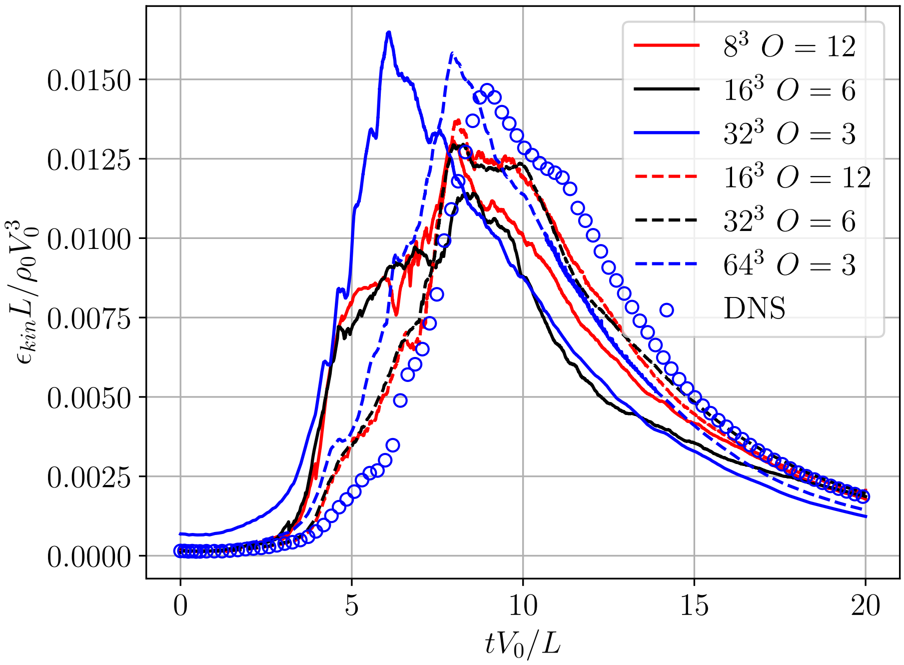

Figure 7: Kinetic energy dissipation for different combinations of mesh size and numerical orders using the BSS method. Solid lines indicate cases with 96^3 total DOFs and dashed lines 192^3 DOF. Red, black, and blue colors indicate simulation respectively with numerical orders of 12, 6, and 3. Solid lines are the simulations performed with LES models, while blue circles are the DNS results.

Figure 7 plots the dissipation of the different mesh and numerical order to highlight how the method performs with different setups. All the cases with 96^3 DOFs have very different dissipation indeed in the 32^3 order 3 the peak dissipation is predicted to occur sooner and with higher intensity. The order 12 case is the one with the best performance, offering more numerical bandwidth to the BSS closure, resulting in a better estimation of turbulent SFS activity. The cases with 192^3 DOFs are closer to the reference DNS resolution and for this reason, the mesh, or the order, have both equally a large impact on the solution with better results achieved refining the mesh, as seen in the shock-vortex interaction case. The largest difference is the peak that is stronger for the order 12 simulation due to a larger Legendre spectral bandwidth available to the model.

Table 2: Time, number of iterations, and the second per iteration all normalized respect to the no model case for TGV simulation with no model, Smagorinsky, Dynamic Smagorinsky, and Legendre Spectral Viscosity (BSS) methods. The results are obtained on a 16^3 elements mesh, numerical order 6, and up to the same physical time in the simulation.

	Wall Time	# iterations	Time per iteration
No model	1.000	1.000	1.000
Smagorinsky	1.009	0.987	1.024
Dynamic Smagorinsky	0.940	0.801	1.173
BSS	1.067	0.990	1.078

Table 2 reports the computational time, the number of iterations, and the time per iteration by all SFS models and a no-model case for a 16^3 mesh size with numerical order 6. As expected, the Dynamic Smagorisky model is the slowest due to the large number of auxiliary filtered quantities needed to estimate the dynamic coefficients. The standard Smagorisky is the one with the lowest overhead. BSS has an intermediate overhead, being 6% slower than the standard one. From the number of iterations it is possible to conclude that all models lead to a lower time constraint induced by the SFS stresses because all of them require fewer iterations than without a model.

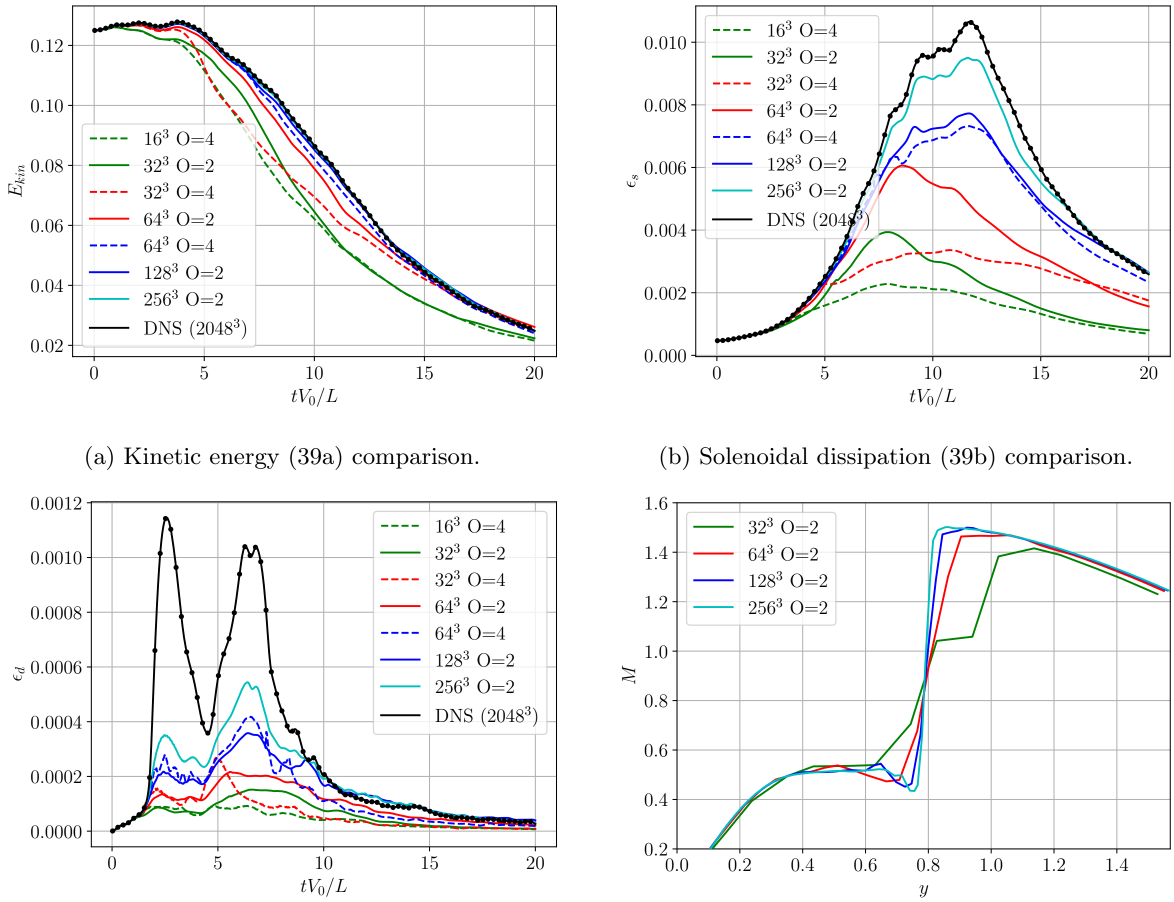

(a) Kinetic energy (39a) comparison.

(b) Solenoidal dissipation (39b) comparison.

(c) Dilatational dissipation (39c) comparison.

(d) Mach profile at $x = 0$, $z = 0$, and $tV_0/L = 2.5$.

Figure 8: BSS results compare to DNS results of Lusher and Sandham [48] in black with circles, while BSS results was represent with solid lines without circles.

5 Subfilter-Scale and shock capturing modeling: Supersonic Taylor-Green Vortex

In the previous sections, the BSS model was validated for its shock capturing (Section 3) and LES capabilities (Section 4). In the current section, the model is tested on a supersonic TGV case that requires subfilter-scale and shock capturing modeling. The flow can be initiliazed using the same equations used for the subsonic TGV case in section 4 but in this case $M_0 = \frac{V_0}{\sqrt{\gamma p_0/\rho_0}} = 1.25$ and $Re = \frac{\rho_0 V_0 L}{\mu_0} = 1,600$. In this investigation, the time is normalized as for the subsonic TGV case and the quantities of interest are:

$$E_{kin} = \frac{1}{2\rho_0 V_0^2 \mid \Omega \mid} \int_\Omega \rho \boldsymbol{u} \cdot \boldsymbol{u} d\Omega \tag{39a}$$

$$\epsilon_s = \frac{L^2}{Re V_0^2 \mid \Omega \mid} \int_\Omega \frac{\mu(\mathrm{T})}{\mu_0} \boldsymbol{\omega} \cdot \boldsymbol{\omega} d\Omega \tag{39b}$$

$$\epsilon_d = \frac{4L^2}{3Re V_0^2 \mid \Omega \mid} \int_\Omega \frac{\mu(\mathrm{T})}{\mu_0} (\nabla \cdot \boldsymbol{u})^2 d\Omega \tag{39c}$$

where Ω is the domain and $\boldsymbol{\omega} = \nabla \boldsymbol{u}$ the vorticity of the flow. In this work different BSS numerical orders and resolutions are compared to the DNS results obtained by Lusher and Sandham [48]. In [37] BSS is compare for the same case to different models.

The simulations were performed on 5 different mesh resolutions (16^3, 32^3, 64^3, 128^3, and 256^3) and two numerical orders (O= 2 and O= 4), so that some cases have the same degrees of freedom and different numerical orders (DOF 64^3, 128^3, 256^3, and 512^3). The 512^3 DOF was investigated only on the O= 2 order because of the high computational cost to investigate the O= 4 case. From figure 8a it is possible to see that among all cases the 64^3 DOF is further from the DNS as expected and that there is not a big difference between the two numerical orders. The biggest difference between numerical orders with the same DOF is for the 128^3 DOF where the O= 2 case is close to the DNS result instead the O= 4 is more dissipative around $tV_0/L = 4.5$. This result is not caused by the model but by the cutoff filter required to simulate these low resolutions. Indeed for the 64^3 and 128^3 DOF the simulations activate a cutoff filter in the elements where there are too many oscillations, filtering down the solution to O= 1 and therefore dissipating more than expected. This effect is in part reduced in the order 2 cases but it still active in some of the elements.

Plots 8b and 8c show the solenoidal and dilational dissipation and it is possible to see how in the low DOF cases the dissipation is significantly underestimated especially when comparing the 128^3 DOF cases. Instead for 256^3 DOF cases, both simulations can get the second peak of dissipation because they only rely on the BSS model and no external filter. It is important to notice that without the BSS model the filtering needs to be applied to a larger number of elements to allow the simulation to finish and it is impossible to run any simulations with a filter or the BSS model. The filter effect is clearly visible in figure 8d where the Mach profile is plotted for all O= 2 cases at $x = 0$, $z = 0$, and $tV_0/L = 2.5$, which correspond to the peak of the dilatational dissipation. Indeed, it is possible to see how the 32^3 elements mesh there is a cell where the shock is cut in half by an order 1 solution. Instead, for the other cases the shock looks smooth but it is important to point out that also for O= 2 the 128^3 still needs a filter to finish the simulation, which is probably not active in that specific place at that specific time in the domain..

6 Conclusion

In this paper, we investigated a new model called Block Spectral Stresses (BSS) method for shock-capturing and LES model in high-order finite volume methods. BSS has been implemented in a block spectral unstructured code called H3AMR and investigated on simulations with shocks and turbulence. In the Sod shock tube case, the model allows to simulate up to numerical order 20, we were not able to reach higher order because of the limitation but the model can potentially allow higher orders. From this investigation, we also notice how the shock is better predicted when the mesh is refined and not as much when the numerical order is increased. Another shock investigation was on the shock-vortex interaction case, where the model demonstrated to be able to capture the shock without altering the shape of the vortex. Also, in this case, the mesh refinement leads to faster convergence than when increasing the numerical order.

For the LES closure, BSS has been compared to the Smagorinsky and dynamic Smagorinsky models, with the second changed to work in a block spectral code. The Taylor-Green vortex was used to test the model in a homogeneous isotropic turbulence. In the case of numerical order 3 BSS is the only model able to estimate the small scale turbulence and avoid the simulation blow-up. For numerical order 6 and 12 and coarse mesh BSS is more dissipative than the other methods but on finer meshes, it is able to reach similar results to the other models. In a supersonic Taylor-Green Vortex where the model is tested on its subfilter-scale modeling and shock capturing capability BSS showed better results when using a finer mesh and low numerical order, similar to previous simulations.

Therefore, even though BSS is not the best model for every kind of flow, it can work with every flow without significant changes in the code, as in the case of dynamic Smagorinsky which requires different averaging for different kinds of flows. Moreover, from this investigation, the model tends to have better results when it has a high mesh refinement than polynomial refinement. Currently, the model has been used for 1D, 2D, and 3D isotropic turbulence investigation. However, further simulations with more complex flow are required to better assess the model in more practical problems.

Acknowledgments

The authors acknowledge support through N00014-21-1-2475 (ONR-MURI, PI: Venkat Raman) and ONR grant nos. N00014-23-1-2560 (Core ONR program, PI: Carlo Scalo) with Dr. Eric Marineau as program manager.

References

[1] Sergei K Godunov and I Bohachevsky. Finite difference method for numerical computation of discontinuous solutions of the equations of fluid dynamics. *Matematičeskij sbornik*, 47(3):271–306, 1959.

[2] Hung T Huynh. A flux reconstruction approach to high-order schemes including discontinuous Galerkin methods. In *18th AIAA computational fluid dynamics conference*, page 4079, 2007.

[3] Hung T Huynh. A reconstruction approach to high-order schemnes including discontinuous Galerkin for diffusion. In *47th AIAA aerospace sciences meeting including the new horizons forum and aerospace exposition*, page 403, 2009.

[4] HT Huynh, Zhi J Wang, and Peter E Vincent. High-order methods for computational fluid dynamics: A brief review of compact differential formulations on unstructured grids. *Computers & fluids*, 98:209–220, 2014.

[5] Niccolò Tonicello, Guido Lodato, and Luc Vervisch. Entropy preserving low dissipative shock capturing with wave-characteristic based sensor for high-order methods. *Computers & Fluids*, 197:104357, 2020.

[6] Guido Lodato, Patrice Castonguay, and Antony Jameson. Structural wall-modeled les using a high-order spectral difference scheme for unstructured meshes. *Flow, turbulence and combustion*, 92:579–606, 2014.

[7] Guido Lodato, Patrice Castonguay, and Antony Jameson. Discrete filter operators for large-eddy simulation using high-order spectral difference methods. *International Journal for Numerical Methods in Fluids*, 72(2):231–258, 2013.

[8] J-B Chapelier, Marta De La Llave Plata, and Eric Lamballais. Development of a multiscale les model in the context of a modal discontinuous galerkin method. *Computer Methods in Applied Mechanics and Engineering*, 307:275–299, 2016.

[9] J-B Chapelier, Guido Lodato, and Antony Jameson. A study on the numerical dissipation of the spectral difference method for freely decaying and wall-bounded turbulence. *Computers & Fluids*, 139:261–280, 2016.

[10] J-B Chapelier and Guido Lodato. A spectral-element dynamic model for the large-eddy simulation of turbulent flows. *Journal of Computational Physics*, 321:279–302, 2016.

[11] David Gottlieb, Chi-Wang Shu, Alex Solomonoff, and Hervé Vandeven. On the Gibbs phenomenon I: Recovering exponential accuracy from the Fourier partial sum of a nonperiodic analytic function. *Journal of Computational and Applied Mathematics*, 43(1-2):81–98, 1992.

[12] Cornelius Lanczos and John Boyd. *Discourse on Fourier series*. SIAM, 2016.

[13] David Gottlieb and Steven A Orszag. *Numerical analysis of spectral methods: theory and applications*. SIAM, 1977.

[14] Jörg Schumacher, Janet D Scheel, Dmitry Krasnov, Diego A Donzis, Victor Yakhot, and Katepalli R Sreenivasan. Small-scale universality in fluid turbulence. *Proceedings of the National Academy of Sciences*, 111(30):10961–10965, 2014.

[15] Sualeh Khurshid, Diego A Donzis, and KR Sreenivasan. Energy spectrum in the dissipation range. *Physical Review Fluids*, 3(8):082601, 2018.

[16] Diego A Donzis and John Panickacheril John. Universality and scaling in homogeneous compressible turbulence. *Physical Review Fluids*, 5(8):084609, 2020.

[17] Victor C. B. Sousa and Carlo Scalo. A unified quasi-spectral viscosity (qsv) approach to shock capturing and large-eddy simulation. *Journal of Computational Physics*, 459:111139, 2022.

[18] Prateek Gupta, Guido Lodato, and Carlo Scalo. Spectral energy cascade in thermoacoustic shock waves. *Journal of Fluid Mechanics*, 831:358–393, 2017.

[19] Prateek Gupta and Carlo Scalo. Spectral energy cascade and decay in nonlinear acoustic waves. *Physical Review E*, 98(3):033117, 2018.

[20] F. Bassi and S. Rebay. A high-order accurate discontinuous finite element method for the numerical solution of the compressible navier–stokes equations. *Journal of Computational Physics*, 131(2):267–279, 1997.

[21] B. Cockburn and C.W. Shu. Tvb runge-kutta local projection discontinuous galerkin finite element method for conservation laws. ii. general framework. *Mathematics of Computation*, 52:411–435, 1989.

[22] Yu Lv. Development of a nonconservative discontinuous galerkin formulation for simulations of unsteady and turbulent flows. *International Journal for Numerical Methods in Fluids*, 92(5):325–346, 2020.

[23] Eric J Ching and Ryan Johnson. Fully conservative discontinuous galerkin method for supercritical, real-fluid flows. In *AIAA SCITECH 2024 Forum*, page 0913, 2024.

[24] David A. Kopriva and John H. Kolias. A conservative staggered-grid chebyshev multidomain method for compressible flows. *Journal of Computational Physics*, 125(1):244–261, 1996.

[25] Kartikey Asthana, Manuel R. López-Morales, and Antony Jameson. Non-linear stabilization of high-order flux reconstruction schemes via fourier-spectral filtering. *Journal of Computational Physics*, 303:269–294, 2015.

[26] Victor C. B. Sousa and Carlo Scalo. A legendre spectral viscosity (lsv) method applied to shock capturing for high-order flux reconstruction schemes. *Journal of Computational Physics*, 460:111157, 2022.

[27] Morduchow M and Libby P. On a complete solution of the one-dimensional flow equations of a viscous, heat-conducting, compressible gas. *J Aeronaut Sci*, 16(11):674–84, 1949.

[28] Joel Smoller. *Shock waves and reaction—diffusion equations*, volume 258. Springer Science & Business Media, 2012.

[29] Manuel D Salas and Angelo Iollo. Entropy jump across an inviscid shock wave. *Theoretical and computational fluid dynamics*, 8(5):365–375, 1996.

[30] JF Colombeau and AY Le Roux. Multiplications of distributions in elasticity and hydrodynamics. *Journal of Mathematical Physics*, 29(2):315–319, 1988.

[31] Pablo Fernandez, Cuong Nguyen, and Jaime Peraire. A physics-based shock capturing method for unsteady laminar and turbulent flows. In *2018 AIAA Aerospace Sciences Meeting*, page 0062, 2018.

[32] F Ducros, P Comte, and M Lesieur. Large-eddy simulation of a spatially growing boundary layer over an adiabatic flat plate at low mach number. *International journal of heat and fluid flow*, 16(5):341–348, 1995.

[33] Carson L. Running, Benjamin L. Bemis, J. Luke Hill, Matthew P. Borg, Joel J. Redmond, Karl Jantze, and Carlo Scalo. Attenuation of hypersonic second-mode boundary-layer instability with an ultrasonically absorptive silicon-carbide foam. *Experiments in Fluids*, 64(4), 2023.

[34] Benjamin L. Bemis, John L. Brun, C. Taber Wanstall, Jonathan L. Hill, Matthew P. Borg, Joel J. Redmond, Matteo Ruggeri, Karl Jantze, Carlo Scalo, and Carson L. Running. Ultrasonically absorptive silicon-carbide foam for boundary-layer control. In *AIAA SCITECH 2023 Forum*, 2023.

[35] Benjamin L. Bemis, Megan C. Sieve, Jonathan L. Hill, Matthew P. Borg, Joel J. Redmond, Matteo Ruggeri, Karl Jantze, Carlo Scalo, and Carson L. Running. Effect of porosity on the ability of silicon-carbide foams to attenuate the second-mode boundary-layer instability. In *AIAA Aviation 2023 Forum*, 2023.

[36] Carson L. Running, Benjamin L. Bemis, J. Luke Hill, Matthew P. Borg, Joel J. Redmond, Karl Jantze, and Carlo Scalo. Attenuation of hypersonic second-mode boundary-layer instability with an ultrasonically absorptive silicon-carbide foam. *Experiments in Fluids*, 64(4):79, 2023.

[37] Jean-Baptiste Chapelier, David J. Lusher, William Van Noordt, Christoph Wenzel, Tobias Gibis, Pascal Mossier, Andrea Beck, Guido Lodato, Christoph Brehm, Matteo Ruggeri, Carlo Scalo, and Neil Sandham. Comparison of high-order numerical methodologies for the simulation of the supersonic Taylor–Green vortex flow. *Physics of Fluids*, 36(5):055146, 05 2024.

[38] David A. Kopriva and John H. Kolias. A conservative staggered-grid chebyshev multidomain method for compressible flows. *Journal of Computational Physics*, 125(1):244–261, 1996.

[39] J. Smagorinsky. General circulation experiments with the primitive equation i the basic experiment. *Monthly Weather Review*, 91:99–164, 1963.

[40] Parviz Moin, Kyle Squires, W Cabot, and Sangsan Lee. A dynamic subgrid-scale model for compressible turbulence and scalar transport. *Physics of Fluids A: Fluid Dynamics*, 3(11):2746–2757, 1991.

[41] V.V. Rusanov. Calculation of interaction of non–steady shock waves with obstacles. *USSR Computational Mathematics and Mathematical Physics*, 1:267–279, 1961.

[42] Massimo Germano, Ugo Piomelli, Parviz Moin, and William H Cabot. A dynamic subgrid-scale eddy viscosity model. *Physics of Fluids A: Fluid Dynamics*, 3(7):1760–1765, 1991.

[43] A survey of several finite difference methods for systems of nonlinear hyperbolic conservation laws. *Journal of Computational Physics*, 27(1):1–31, 1978.

[44] Takanori Haga and Soshi Kawai. On a robust and accurate localized artificial diffusivity scheme for the high-order flux-reconstruction method. *Journal of Computational Physics*, 376:534–563, 2019.

[45] Hiroshi Terashima, Soshi Kawai, and Mitsuo Koshi. Consistent numerical diffusion terms for simulating compressible multicomponent flows. *Computers Fluids*, 88:484–495, 2013.

[46] Janet L. Ellzey, Michael R. Henneke, J. Michael Picone, and Elaine S. Oran. The interaction of

a shock with a vortex: Shock distortion and the production of acoustic waves. *Physics of Fluids*, 7:172–184, 1995.

[47] Audrey Rault, Guillaume Chiavassa, and Rosa Donat. Shock-vortex interactions at high mach numbers. *Journal of Scientific Computing*, 19:347–371, 2003.

[48] David J Lusher and Neil D Sandham. Assessment of low-dissipative shock-capturing schemes for the compressible taylor–green vortex. *AIAA Journal*, 59(2):533–545, 2021.